



Full Length Article

Vanadium induces Ni-Co MOF formation from a NiCo LDH to catalytically enhance the MgH₂ hydrogen storage performance

Zexuan Yang^a, Yazhou Wang^a, Xia Lin^a, Yongjin Zou^{a,*}, Cuili Xiang^{a,*}, Fen Xu^a, Lixian Sun^a, Yong Shen Chua^b

^aGuangxi Key Laboratory of Information Materials, Guilin University of Electronic Technology, Guilin 541004, China

^bSchool of Chemical Sciences, Universiti Sains Malaysia, Minden, Penang 11800, Malaysia

Received 11 November 2024; received in revised form 29 December 2024; accepted 14 January 2025

Available online 3 February 2025

Abstract

Magnesium-based hydrogen storage materials, such as MgH₂, have attracted considerable attention because of its superior hydrogen storage capacities, inexpensive, and excellent reversibility. However, their high thermodynamic stabilities and slow kinetics lead to relatively high desorption temperatures, which severely limit the wide application of MgH₂. In this study, the inclusion of vanadium induced the formation Ni-Co metal-organic frameworks (MOF) from a NiCo layered double hydroxide (LDH), thereby increasing the number of defects and vacancies, and improving the hydrogen storage properties of MgH₂. The synthesized NiCo-MOF/V-O-doped MgH₂ system demonstrates excellent hydrogen storage capacity. More specifically, 5 wt.% of H₂ was released over 20 min at a relatively low dehydrogenation temperature of 250 °C, and almost complete dehydrogenation was achieved at 300 °C for 5 min. In addition, at 125 °C, the hydrogen storage material absorbed 5.5 wt.% H₂ in 10 min. Furthermore, the activation energy of dehydrogenation was determined to be 69.588 ± 6.302 kJ ·mol⁻¹ which is significantly lower than that of the ball-milled MgH₂ (i.e., 118.649 ± 2.825 kJ ·mol⁻¹). It was therefore inferred that during dehydrogenation process, a Mg₂Ni/Mg₂NiH₄ hydrogen pump is formed by Ni, while the V-H and Co-H bonds formed by Co and V during the reaction act synergistically to catalyze the absorption and desorption of hydrogen, thereby increasing the hydrogen storage capacity of MgH₂. These experiments provide new perspectives on the commercial application of MgH₂.

© 2025 Chongqing University. Publishing services provided by Elsevier B.V. on behalf of KeAi Communications Co. Ltd.

This is an open access article under the CC BY-NC-ND license (<http://creativecommons.org/licenses/by-nc-nd/4.0/>)

Keywords: NiCo; MgH₂; V-O.

1. Introduction

In recent decades, the energy crisis and global warming have fueled the growing demand for non-polluting and renewable energy [1–3]. As a non-polluting and efficient energy resource, hydrogen (H₂) has provided an important alternative to the depleting fossil fuels and plays important role in facilitating the nation moving towards a carbon-neutral society [4–7]. Hydrogen is the most abundant element in the

universe, and its product of combustion is only water [8–10]. In addition, hydrogen energy can be stored and transported, which are its main advantages [11–13]. As previously reported, solid hydrogen storage is a prominent and safe initiatives of safely supplying hydrogen energy with a plentiful storage capacity [14–19]. Indeed, Among the three existing hydrogen storage methods, namely high-pressure compression, liquefaction, and solidification, solid-state hydrogen storage allows the highest volumetric hydrogen storage density [20,21]. As an instance, the ordinary density of hydrogen gas is 1191 instances lesser than the volumetric hydrogen storage density of MgH₂, which could exceed 106 kg H₂ per cubic meter, 1.5 times bigger than that of liquid hydrogen and 2.7 times higher than that of hydrogen compressed at 70

* Peer review under the responsibility of Chongqing University.

* Corresponding authors.

E-mail addresses: zouy@guet.edu.cn (Y. Zou), xiangcuili@guet.edu.cn (C. Xiang).

Mpa [22]. In addition, solid-state hydrogen storage permits the storage of hydrogen at ambient temperature and pressure in an easily sealed storage tank, it can improve the safety of hydrogen storage and transit [23–25]. A solid-state hydrogen storage container can immediately lower the circulation speed and amount of hydrogen spills even in an emergency, giving you crucial extra time to take protective action [19]. Currently, MgH₂ is among the most intriguing material for hydrogen storage, and is characterized by its higher gravimetric and volumetric and volumetric capacity, highly abundance, lighter weight and lower cost as compared to other metal hydrides [26–28]. However, MgH₂ exhibits sluggish hydrogen absorption and desorption kinetics at moderate temperatures and high thermodynamic stability [29–32]. Consequently, the practical use of MgH₂ has been constrained, prompting numerous efforts to address these problems, including alloying [33–38], nanosizing [39,40], catalyst doping [41–44], and the exploration of thin-film technologies [45]. In addition, mechanical milling has been demonstrated to reduce the particle size to improve the dehydrogenation performance of magnesium hydride matrix [46–49], inducing defects, disrupting the MgO layer and exposing the fresh Mg surface for hydrogenation [50].

Previous studies have demonstrated that the introduction of catalysts is a viable method for improving the hydrogen storage performance of MgH₂. In particular, transition metals (Ti, V, Mn, Nd, Mn, etc.) and their compounds have a significant effect on MgH₂. Liang et al. [51] studied the adsorption characteristics of MgH₂ and established that different transition metals have corresponding catalytic effects on MgH₂. Among them, the catalytic effect of V was the best. DFT calculations revealed that the length of the Mg-H bond in pure MgH₂ is 1.714 Å; by introducing metallic V or V₂O₃ catalyst, the length of the Mg-H bond can be extended to 3.116 Å and 2.046 Å, respectively [52]. Lengthening the bond length is more favorable for H desorption. In recent years, interest in MOF materials has gradually increased due to their high specific surface area, unique pore structure, and good gas adsorption and storage ability. Lu et al. [53] investigated the effect of V-based MOFs on the H storage properties of MgH₂. Their research revealed that the addition of 7 wt.% V-MOF to MgH₂ reduced the starting H release temperature by 150 °C; moreover, the activation energies of H absorption and release were reduced to 30.3 ± 2.1 and 98.4 ± 2.9 kJ ·mol⁻¹, respectively.

Although V has been widely used to enhance the hydrogen storage capacity of MgH₂, there is little literature on the implementation of V-induced MOF for this purpose. In this study, for the first time, a vanadate solution was used to transform the bilayer of LDH into a new monolayer porous structure. The homogeneous loading of vanadium's multivalent oxides onto the MOF by solvent heating resulted in the formation of abundant vacancies and defects, which improved the hydrogen uptake and discharge properties of MgH₂, thus providing an opportunity for multifaceted study of the application of MgH₂.

2. Experimental section

2.1. Materials

Cobalt nitrate hexahydrate (Co(NO₃)₂·6H₂O, AR, 99%), nickel nitrate hexahydrate (Ni(NO₃)₂·6H₂O, AR, 99%), and 2-methylimidazole (C₄H₆N₂, AR, 99%) were purchased from Xilong Scientific Co., Ltd. (China). Ethanol (AR, 99.5%), and ammonium metavanadate (NH₄VO₃, AR, 99%) were purchased from the Aladdin Chemical Co., Ltd. (China). Magnesium hydride (MgH₂, 99.89% purity) was supplied by Shanghai Magnesium Source Power Technology Co., Ltd. (China). MgH₂ (200 mesh, 98%) was procured from Shanghai Magnesium Technology Co., Ltd.

2.2. Synthesis of the ZIF-67 precursor, NiCo LDH, and NiCo-MOF/V-O species

Co(NO₃)₂·6H₂O and C₄H₆N₂ at a molar ratio of 4:1 were dissolved in methanol (40 mL), mixed and stirred at room temperature for 1 h, and then allowed to stand for 24 h to finally form the desired ZIF-67 precursor. Subsequently, Ni(NO₃)₂·6H₂O was added at 60 °C and stirring was continued. In this reaction, C₄H₆N₂ was employed as a common hydrolyzing agent to release large amounts of carbonate, which may contribute to the formation of a highly crystalline NiCo layered double hydroxide (LDH) [54,55]. Finally, the prepared NiCoLDH was introduced to a (NH₄)VO₃ saline and heated at 150 °C for 3 h to yield the desired NiCo-MOF/V-O composite system (Fig. 1), where V-O denotes a multivalent mixture of oxides of V.

2.3. Synthesis of the MgH₂—xNiCo-MOF/V-O (x = 5, 7 and 9) composites

The desired quantity of the prepared NiCo-MOF/V-O catalyst (i.e., 5, 7, 9 wt.%) was mixed with MgH₂ via a mechanochemical procedure in an inert Ar environment using a QM-3SPO4 high-energy planetary ball mill (Nanjing Nanda Instrument Co.). Milling was conducted at a rotational speed of 400 rpm at 15-minute milling intervals followed by 5-minute rest for 15 h under Ar gas at a ball-to-powder weight ratio of 40:1. The samples obtained from the experiment were labeled as MgH₂—xNiCo-MOF/V-O, where x represents the proportion of NiCo-MOF/V-O in each sample. Control samples were prepared by ball milling, in which MgH₂ was milled alone (undoped) and mixed with NiCo-MOF/V-O. The samples were labeled as-milled MgH₂ and MgH₂—xNiCo-MOF/V-O.

2.4. Characterization

X-ray diffraction (XRD) analysis was performed to evaluate the phase compositions of the NiCo-MOF/V-O and the composite materials using a Rigaku SmartLab instrument with Cu K α radiation at 45 KV and 200 mA, with a scan rate of 5° min⁻¹. The microstructures and elemental distributions of the

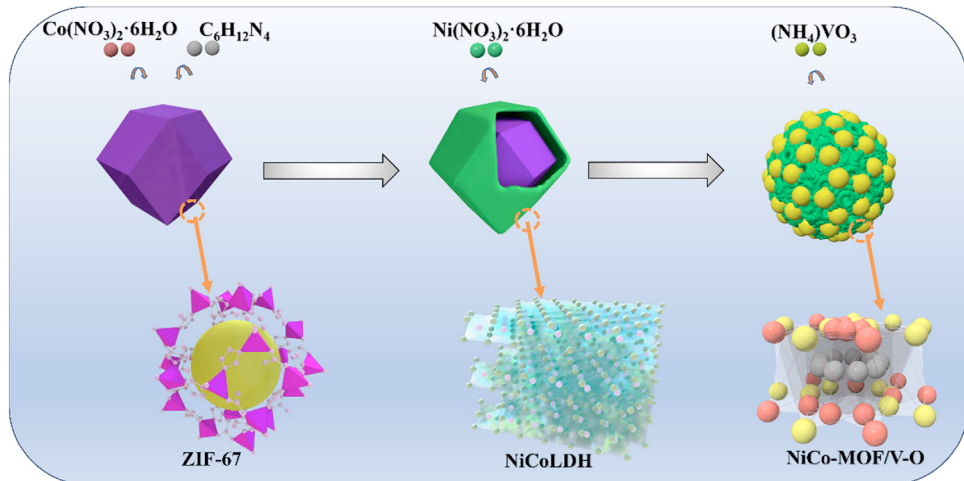


Fig. 1. Synthesis of NiCo-MOF/V-O composite system.

catalysts were examined via transmission electron microscopy (TEM; Talos F200X, USA) and scanning electron microscopy (SEM; JSM-7610F, JEOL Ltd, Japan). X-ray photoelectron spectroscopy (XPS; Thermo Fisher ESCALAB 250Xi) was employed for compositional and elemental analysis. The hydrogen storage performance was assessed using an Automated High Pressure Sieverts Apparatus (HPSA) and an improved Benedict–Webb–Rubin equation of state was used to calculate the hydrogen storage capacity. To ensure system precision, the temperature and pressure were monitored using two high-precision pressure sensors (0.002% FS output resolution) and three Pt100 thermocouples. The initial pressures for hydrogen absorption and desorption were set as 3 MPa for the absorption and desorption measurements. To prevent oxidation, all the samples were manipulated within a glovebox with water vapor and O₂ contents of <0.1 ppm.

3. Results and discussion

3.1. Structure and morphology of the NiCo-MOF/V-O catalyst

Fig. 2(a) displays the XRD spectra for the acquired NiCoLDH and NiCo-MOF/V-O; herein, the diffraction peaks at 2θ values of 18.9, 33.1, 59.1 were ascribed to the (006), (012), (110) planes of Ni(OH)₂ phase (PDS #No.01–1047), proving the successful synthesis of NiCoLDH [56,57]. Moreover, the peak at the 2θ value of 63.0°, corresponding to the (111) plane of the V₃O₄ phase (PDS #No.34–0615), confirmed the successful synthesis of NiCo-MOF/V-O. In Fig. S1 of the support material, detailed peak assignments and phase identification were performed on the XRD analysis to dequantify the phase composition. Additionally, the XPS result of V presented in **Fig. 2(b)** shows characteristic peaks at 525, 523.3, 530.6 and 532.8 eV [58], which can be ascribed to V⁴⁺ 2p_{1/2}, V⁴⁺ 2p_{3/2}, O1, and O3, where the presence of O1 and O3 is attributed to lattice O and O atoms adsorbed on the

surface of the material, respectively. According to XRD and XPS results, the V in NiCo-MOF/V-O changed its valency state from that detected in the V salt, further verifying the presence of VO and VO₂ [59,60]. In **Fig. 2(c)**, the XPS spectra of Co 2p is shown, where the characteristic peaks at 780.2 and 804 eV correspond to the zero-valence states of Co⁰ 2p_{3/2} and Co⁰ 2p_{1/2} [61]. Located near the characteristic peaks at 787.6 and 796 eV, the divalent states of Co²⁺ 2p_{3/2} and Co²⁺ 2p_{1/2} were also present. These data confirm the presence of Co in the form of NiCo-MOF/V-O. As shown in **Fig. 2(d)**, the binding energies in the prepared samples having binding energies at the vicinity of 855.36 and 857 eV correspond to Ni²⁺ 2p_{3/2} and Ni³⁺ 2p_{3/2}, respectively, and the binding energies at the vicinity of 866 and 873.07 eV correspond to Ni²⁺ 2p_{1/2} and Ni³⁺ 2p_{1/2} [62,63], respectively. In addition, the peaks observed at 861.31 and 878.3 eV were the corresponding satellite peaks affected by dithering, denoted by the acronym Sat. These data confirmed the change in valency of Ni in NiCo-MOF/V-O.

The morphologies of ZIF-67 precursor, NiCoLDH and NiCo-MOF/V-O, were characterized by SEM; their corresponding SEM images are shown in **Figs. 3(a)–(d)**. In **Fig. 3(a)**, we can clearly see the dodecahedral structural morphology of the ZIF-67 precursor, which indicates that ZIF-67 precursor was successfully synthesized. **Fig. 3(b)** shows the bilayer structure of NiCoLDH; combined with the XRD results, it can be established that NiCoLDH was successfully synthesized. Finally, in **Figs. 3(c, d)**, it is observed that in NiCo-MOF/V-O, which was generated by the induction of V composites, the original bilayer structure of NiCoLDH disappeared and was replaced by a spherical structure with more pores, and the outer spheres were loaded V-O. Combined with the XRD results, this confirms that NiCoMOF/V-O was successfully synthesized. Moreover, the TEM images shown in **Figs. 3(e) and 3(f)** demonstrate a uniform dispersion in NiCo-MOF/V-O, with particle sizes of <20 nm, while the HRTEM image in **Fig. 3(g)** shows that NiCo-MOF/V-O possesses lattice edge spacings of 0.41 nm. Additionally, **Fig. 3(f)** displays

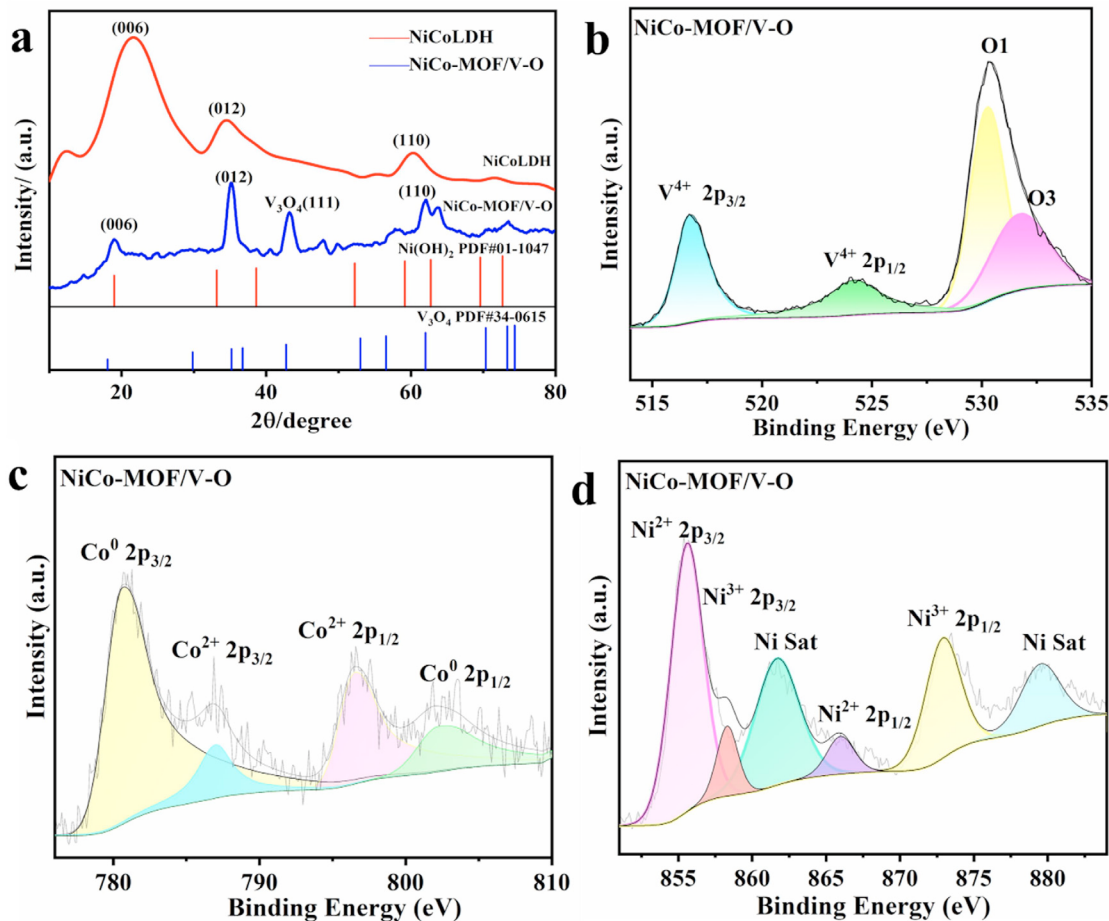


Fig. 2. (a) XRD patterns, (b) high-resolution XPS spectra of V^{4+} 2p_{1/2} and V^{4+} 2p_{3/2}, (c) high-resolution XPS spectra of Co^0 2p_{1/2}, Co^0 2p_{3/2} and Co^{2+} 2p_{3/2}, Co^{2+} 2p_{1/2}, (d) high-resolution XPS spectra of Ni^{2+} 2p, Ni^{3+} 2p and Ni sat.

the EDS results which reveal uniform distribution of Ni, Co, V, and O in the prepared NiCo-MOF/V-O.

3.2. Catalytic effects of NiCo-MOF/V-O on hydrogen storage performance of MgH_2

To clarify how NiCo-MOF/V-O affects the dehydrogenation and hydrogenation efficiency of MgH_2 , different loadings of NiCo-MOF/V-O were doped on MgH_2 via ball milling. The temperature programmed desorption (TPD) curves of the resulting samples are shown in Fig. 4(a). Compared with the unmodified MgH_2 , the addition of NiCoLDH or NiCo-MOF/V-O significantly reduced the initial temperatures of dehydrogenation in the MgH_2 system. More specifically, samples containing 5, 7, and 9 wt.% NiCo-MOF/V-O exhibited initial dehydrogenation temperatures of 190, 155, and 153 °C, respectively. Notably, the initial dehydrogenation temperature of the sample containing 7 wt.% NiCo-MOF/V-O is ~125 °C lower than that of unmodified MgH_2 . More importantly, complete dehydrogenation can be achieved upon reaching 300 °C. As compared to NiCoLDH which represents the sample in the absence of V, 25 °C reduction in the initial dehydrogenation temperature can be detected, suggesting an important role of

polyvalent V in further lowering the dehydrogenation temperatures of MgH_2 .

More specifically, during isothermal dehydrogenation, the sample containing 7 wt.% NiCo-MOF/V-O achieved almost complete dehydrogenation, reaching 6.5 wt.% H₂ within 5 min at 300 °C (Fig. 4(b)). Under the same temperature, the as-milled MgH_2 released only 0.5 wt.% H₂ (Fig. 4(d)) in 30 min. Isothermal hydrogenation at 20 MPa H₂ shown in Fig. 4(c) demonstrated that the dehydrogenated 7 wt.% NiCo-MOF/V-O modified MgH_2 can absorb ~5.4 wt.% H₂ within 20 min at temperature as low as 100 °C. In contrast, the dehydrogenated as-milled MgH_2 showed only a negligible absorption of 0.6 wt.% in 60 min at a higher temperature of 150 °C. In summary, NiCo-MOF/V-O modified MgH_2 demonstrated remarkable improvement in the both hydrogenation and dehydrogenation kinetics as compared to the NiCoLDH modified MgH_2 and as-milled MgH_2 , suggesting that induction by the salt solution of V, which exhibits a lower onset hydrogen release temperature and much improved catalytic performance compared to the catalysts without added V.

To more comprehensively investigate the dehydrogenation kinetics of the 7 wt.% NiCo-MOF/V-O modified MgH_2 , the apparent activation energy (E_a) for dehydrogenation was

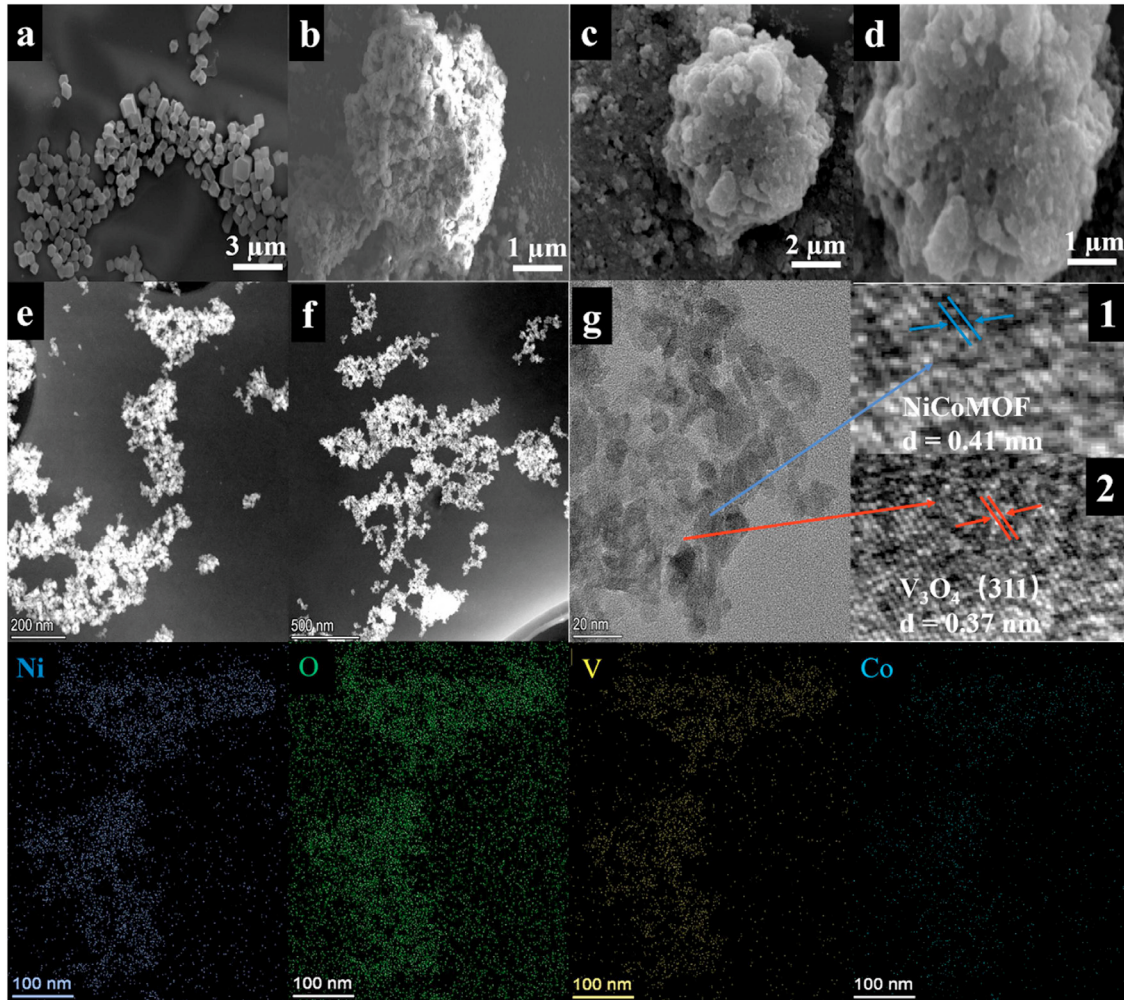


Fig. 3. (a) SEM images of ZIF-67 precursor, (b) SEM images of NiCoLDH, (c, d) SEM images of NiCo-MOF/V-O (e,f) TEM image, (g) HRTEM image, and (1,2) HAADF and matching photos from the EDS elemental mapping.

computed. The JMAK equation was used to model the isothermal dehydrogenation data [64,65]:

$$\ln [-\ln (1 - \alpha)] = n \ln k + n \ln t,$$

where n is the Avrami exponent, k is the effective kinetic parameter, and α is the reaction fraction of MgH₂ transformed into Mg at time t . As shown in Figs. 5(a) and (c), the JMAK plots for the 7 wt.% NiCo-MOF/V-O modified MgH₂ and the as-milled MgH₂ were fitted to determine the values of n and $n \ln k$. The resulting rate constant, k , was utilized to determine the activation energy for the dehydrogenation reaction using the Arrhenius equation (Figs. 5(b) and (d)) [66]:

$$k = A \exp(E_a/RT),$$

where A , R , and T , are the pre-exponential factor, the gas constant, and the temperature, respectively. Consequently, the dehydrogenation activation energy of the MgH₂ system containing 7 wt.% NiCo-MOF/V-O was calculated to be 69.588 ± 6.302 kJ·mol⁻¹, which is less than the MgH₂ system containing 7 wt.% NiCoLDH (105.005 ± 0.748 kJ·mol⁻¹) by 33.8% (Figs. 5(b) and 5(d)) and as-milled MgH₂

(i.e., 118.649 ± 2.825 kJ·mol⁻¹) by 58.5% (Figs. 5(e) and 5(f)). The calculated activation energies for 5 wt.% NiCo-MOF/V-O -MgH₂ and 9 wt.% NiCo-MOF/V-O -MgH₂ were 71.085 ± 1.530 kJ·mol⁻¹ and 67.343 ± 5.728 kJ·mol⁻¹, respectively (Fig. S3). These data enable the kinetic effects of different doping ratios of E_a on MgH₂ to be fully elucidated. The participation of NiCo-MOF/V-O in the dehydrogenation of MgH₂ improves the dehydrogenation kinetics of the composite by drastically lowering the energy barrier. Moreover, the obtained results confirm that the dehydrogenation activation energy of the composite is lower than those of MgH₂ systems.

To evaluate the stability of the NiCo-MOF/V-O catalyst, the composite underwent cyclic assessments of performance. At 325 °C (Fig. 6), it was found that the sample's first H absorption capacity was 7.597 wt.%, while the first emission of H was just 6.494 wt.%. The H absorption and desorption capacity after the subsequent two cycles dropped to 7.589 and 6.451 wt.%, respectively, and these values stayed largely constant for up to 30 cycles, decreasing only slightly to 7.239 and 6.295 wt.%, respectively. Based on these find-

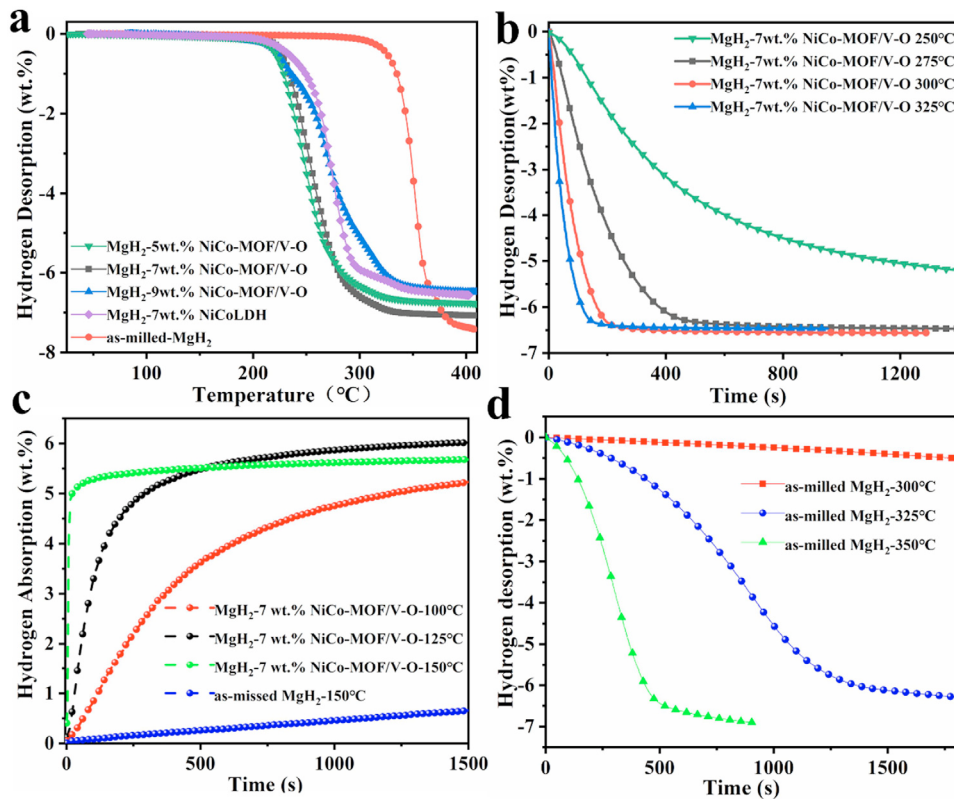


Fig. 4. (a) TPD curves of milled MgH₂ and 7 wt.% NiCoLDH -MgH₂ and x wt.% NiCo-MOF/V-O-MgH₂ (x = 5, 7, 9). (b) Isothermal desorption curves of 7 wt.% NiCo-MOF/V-O-MgH₂. (c) Isothermal hydrogenation curves of 7 wt.% NiCo-MOF/V-O-MgH₂ composite at different temperatures. (d) Isothermal desorption curves of as-milled-MgH₂.

ings, the predicted effective hydrogen capacity was ~97.5%, which demonstrated the extremely stable and efficient nature of NiCo-MOF/V-O for such applications. In Supporting Information Fig. S2, error bars and standard deviation data statistics for the cycling data of 7 wt.% NiCo-MOF/V-O -MgH₂ at 325 °C are presented to better visualize the cycling error.

Subsequently, the thermodynamic performance of 7 wt.% NiCo-MOF/V-O-MgH₂ and as-milled MgH₂ samples were comprehensively evaluated, as shown in the pressure-composition-temperature (PCT) curves presented in Figs. 7(a) and (b), respectively. The PCT curves reveal that the plateau pressures during dehydrogenation of the composite at 300, 325, and 350 °C were 1.20, 2.45, and 5.21 bar, respectively whereas those during hydrogen absorption were 2.92, 4.65, and 7.30 bar, respectively. Based on the dehydrogenation/rehydrogenation plateau pressures at various temperatures, the enthalpy (ΔH) changes were computed using the Van't Hoff equation [67]:

$$\ln(P/P_0) = \Delta H/RT - \Delta S/R$$

where P is the PCT curve's plateau pressure, P_0 is the standard atmospheric pressure, ΔH and ΔS are the enthalpy and entropy changes, respectively, R is the gas constant, and T is the temperature at which the PCT test was performed. Using this equation, the enthalpies (ΔH) of hydrogen absorption and desorption for the composite were determined to be 61.615 ± 0.499 kJ·mol⁻¹ and 82.308 ± 5.071 kJ·mol⁻¹, re-

Table 1
Hydrogen storage performance of 7 wt.% NiCo-MOF/V-O-MgH₂ composite and other identically doped MgH₂ materials.

Sample	Onset Temperature (°C)	E_a (kJ/mol)	E_a (as milled-MgH ₂) (kJ/mol)	Ref
MgH ₂ -7 wt.% NiCo-MOF/V-O	155	69.45	118.65	This work
MgH ₂ -7 wt.% MOFs-V	190.6	98.4	157.5	[53]
MgH ₂ -7 wt.% N- LaTiO ₃	193	91.2	122.86	[68]
MgH ₂ -7 wt.% Ti ₃ AlC ₂ MAX-phase	236	114.82	144	[69]
MgH ₂ -7 wt.% Nb ₂ O ₅ @MOF	181.9	75.57	140.51	[70]
MgH ₂ -7 wt.% Fe-V	218	103.6	144.4	[71]
MgH ₂ -7 wt.% V _{NS}	187.2	119.3	154.6	[72]
MgH ₂ -7 wt.% TiNb ₂ O ₇	177	96	139	[73]

spectively (Figs. 7(a) and (b)), indicating that NiCo-MOF/V-O has little effect on the thermodynamic properties of MgH₂.

Table 1 summarizes the hydrogen storage performance of the MgH₂-7 wt.% NiCo-MOF/V-O composite in the present study and other identically doped MgH₂ materials reported in the literature. By comparing the indicators, the superior hydrogen storage performance of MgH₂-7 wt.% NiCo-MOF/V-O is firmly established.

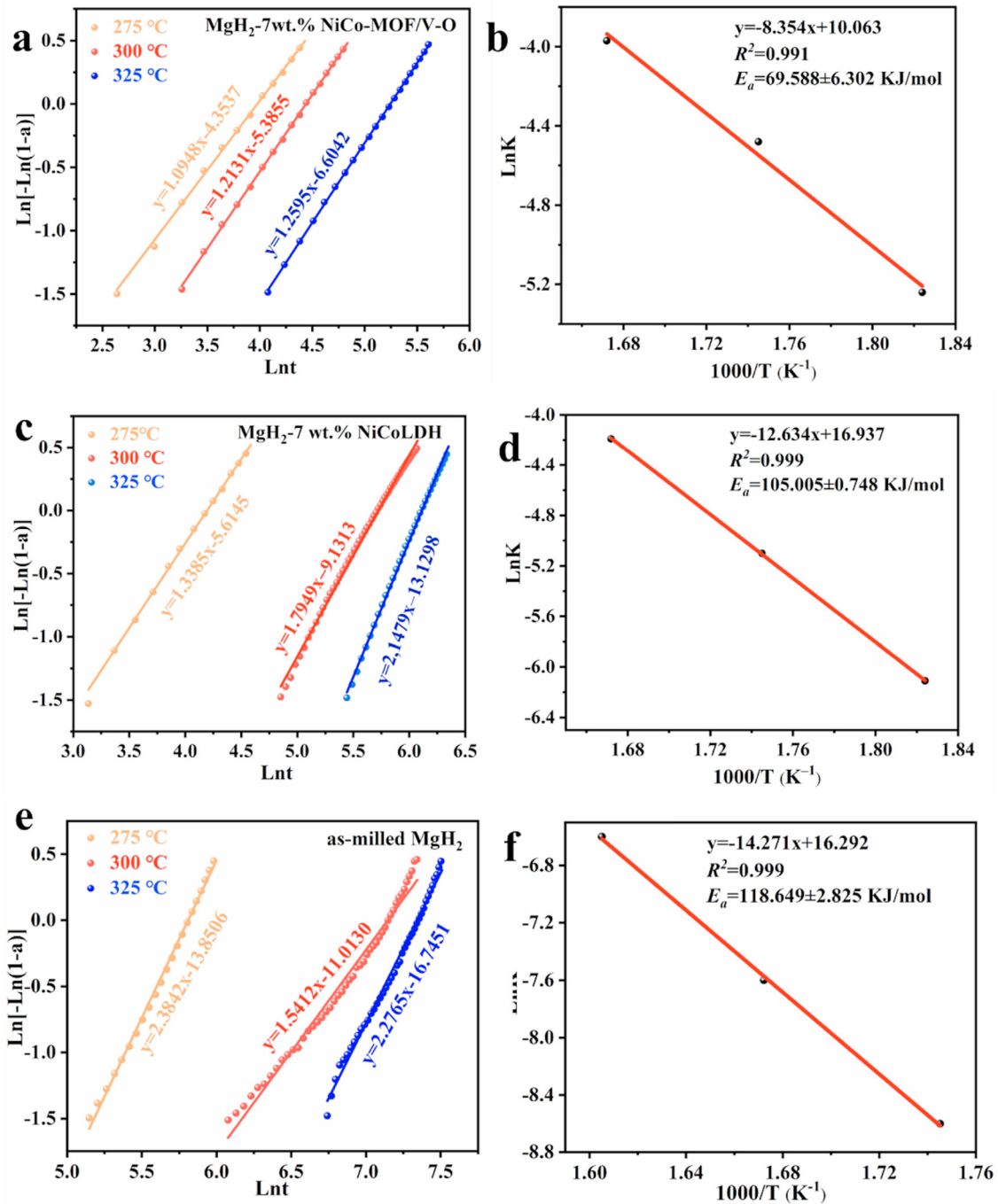


Fig. 5. JMAK plots for the dehydrogenation process and the corresponding Arrhenius plots for (a, b) 7 wt.% NiCo-MOF/V-O-MgH₂, (c, d) 7 wt.% NiCoLDH-MgH₂ and (e, f) as-milled MgH₂.

3.3. Tentative catalytic mechanism

To clarify the role of NiCo-MOF/V-O in the dehydrogenation/hydrogenation of MgH₂, followed by XRD characterization and dehydrogenation/hydrogenation studies. The XRD patterns of the dehydrogenated and hydrogenated samples are displayed in Fig. 8(a). Peaks corresponding to both the NiCoLDH and V-O are easily discernible in the ball-milled sample. The samples after dehydrogenation clearly demonstrates the presence of not only metallic magnesium, but also

V₂O₃ as results of the reaction between V with Mg. Mg₂Ni was detected in both hydrogen absorption and release, indicating that the Ni in the catalyst was destroyed during hydrogen absorption and release. In addition, the XRD pattern of V-O was found to exhibit significant changes after dehydrogenation/hydrogenation. More specifically, the disappearance of V-O after the release of hydrogen may be due to the formation of V-H bonds during the reaction, along with a simultaneous lowering of the activation energy. Further XPS measurements were carried out on a similar composite con-

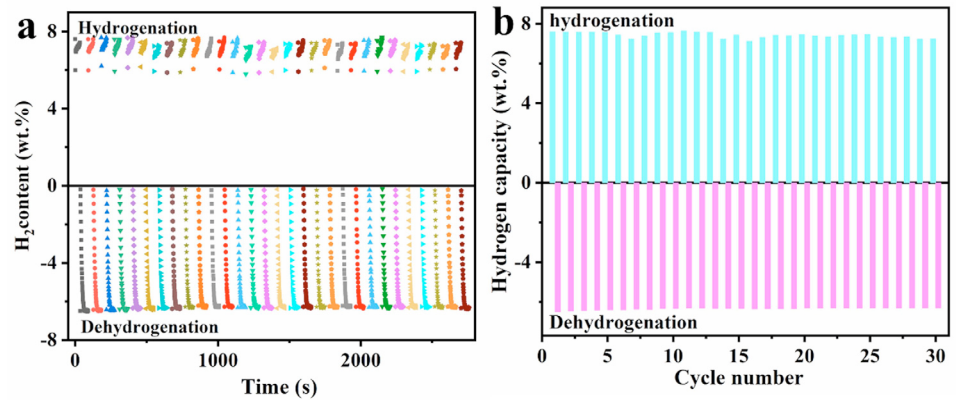


Fig. 6. Isothermal dehydrogenation kinetics curves of 7 wt.% NiCo-MOF/V-O -MgH₂ at 325 °C.

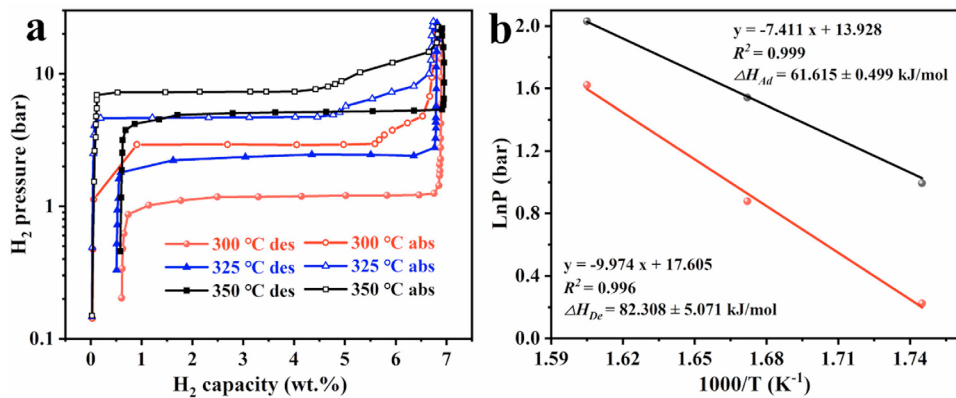


Fig. 7. PCT (pressure-composition-temperature) curves for hydrogen desorption at various temperatures and (f) an't Hoff plots of 7 wt.% NiCo-MOF/V-O-MgH₂.

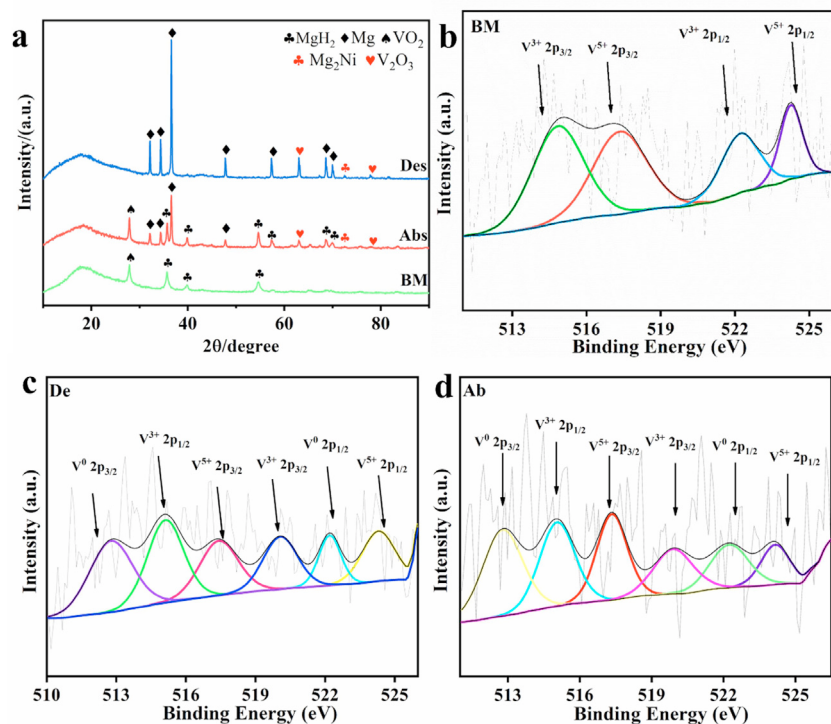


Fig. 8. XRD patterns of 7 wt.% NiCo-MOF/V-O-MgH₂ in dissimilar conditions: (a) XPS spectra of V 2p in the 20 wt.-% NiCo-MOF/V-O -MgH₂ sample at Ball-Milled (BM), Desorption (Des), and Absorption (Abs) (b-d).

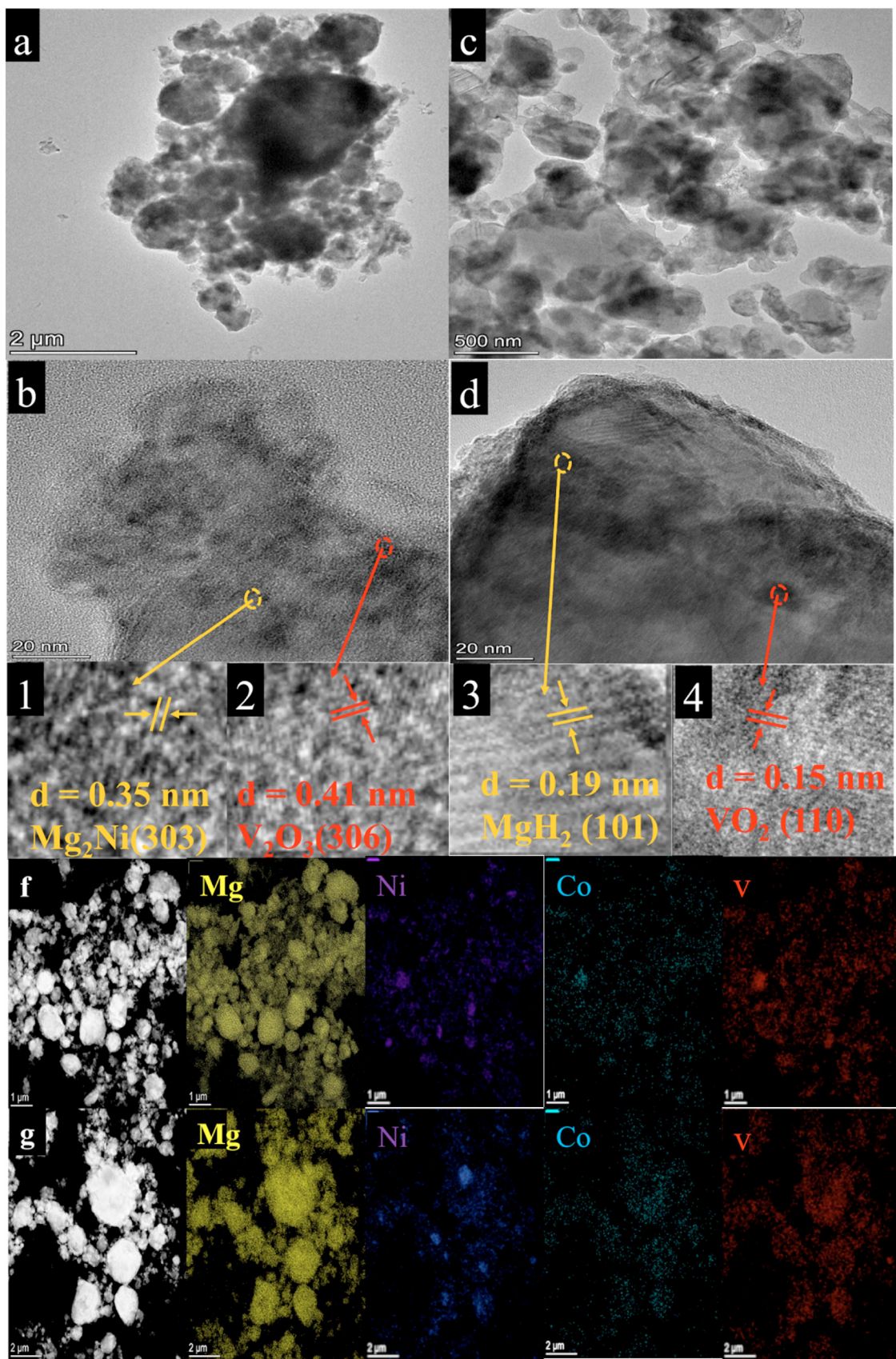


Fig. 9. (a-d) TEM of 20 wt.% NiCo-MOF/V-O-MgH₂, (a,b) sample of Desorption (Des) and (c,d) Absorption (Abs), (e, f) TEM-EDS of 20 wt.% NiCo-MOF/V-O-MgH₂ sample of Desorption (g), (Des) and Absorption (f), (Abs).

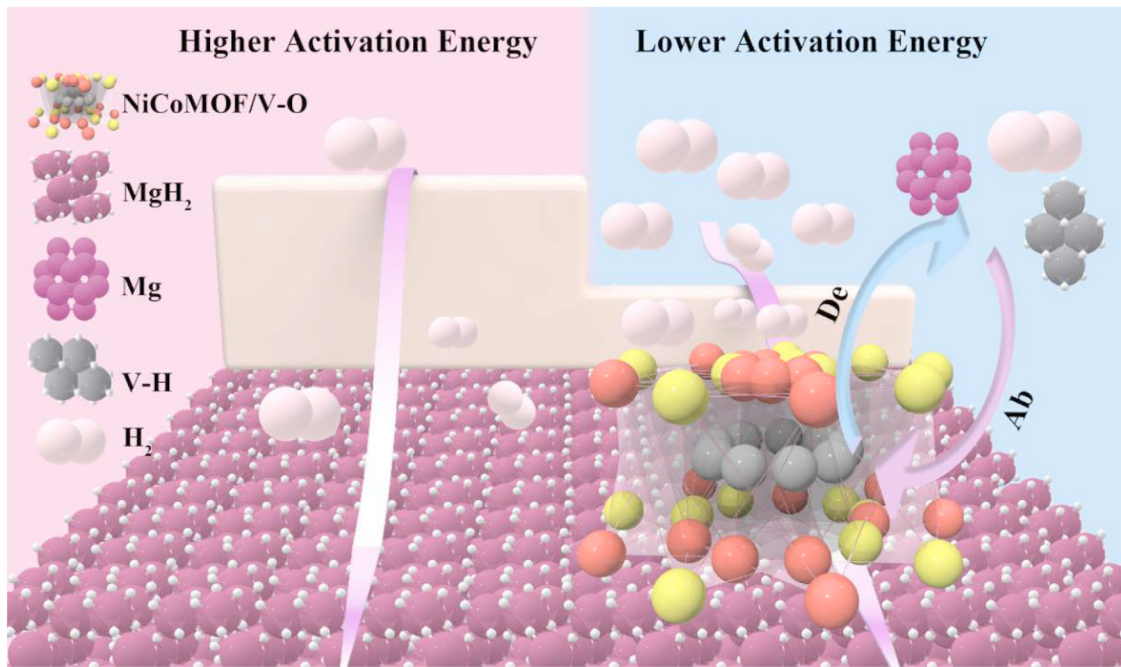


Fig. 10. Schematic of the hydrogenation/dehydrogenation of MgH_2 catalyzed by NiCo-MOF/V-O.

taining 20 wt.% NiCo-MOF/V-O composite to benefit further information about the condition of the internal vanadium component during cycling. Figs. 8(b)–8(d) present the XPS spectra of the V 2p orbital after ball milling and hydrogen absorption/desorption. It can be seen that following ball-milling, V^{4+} was converted to V^{5+} (524.31, 517.35 eV) and V^{3+} (515.00, 522.21 eV), while during dehydrogenation, V-O further reacts with MgH_2 to form multivalent states of V, such as V^0 (512.87, 522.21 eV), V^{3+} (515.00, 519.80 eV), and V^{5+} (517.35, 523.31 eV) [74–77]. In addition, during hydrogen absorption, V is reduced to V^0 (512.87, 522.21 eV), V^{3+} (515.00, 519.80 eV), and V^{5+} (517.35, 523.31 eV). Furthermore, the obtained results show that the introduction of V can decrease the Mg–H bond strength effectively lowering the dehydrogenation activation energy of MgH_2 . Furthermore, the microstructure and composition of the composite containing 20 wt.% NiCo-MOF/V-O were also examined using TEM-EDS.

TEM images shown in Figs. 9(a-d), it was found that the crystal face spacing of the crystals increased after Desorption, which may be resulted from the development of various defects and voids after Desorption. After hydrogen absorption, the crystal face gap decreased, resulting in agglomeration, and hindering subsequent hydrogen release. Figs. 9(1,2) demonstrates that in the dehydrogenated sample, lattice fringes with lattice spacings of 0.35 nm and 0.41 nm, corresponding to the planes of $\text{Mg}_2\text{Ni}(303)$ and $\text{V}_2\text{O}_3(306)$, Figs. 9(3,4) show that in the hydrogen-absorbed sample, lattice fringes with lattice spacings of 0.15 nm and 0.19 nm, corresponding to the lattice fringes of $\text{V}(110)$ and $\text{MgH}_2(101)$. Figs. 9(f, g) illustrates the elements present after absorption and discharge.

In summary, after dehydrogenation/hydrogenation, as illustrated in Fig. 10, V-induced NiCoLDH changes into NiCo-

MOF, the bilayer LDH transforms into a surface monolayer structure, and the hindering chemical bonds in the middle of the bilayer LDH (Fig. 3) completely disappear. With the addition of NiCo-MOF/V-O catalyst and after ball milling, the samples contain $\text{Mg}_2\text{V}_2\text{O}_7$, as confirmed by the XRD spectrum shown Fig. 8(a). Figs. 8(b) and 2(b) verify the change in the valence state of the elements after ball-milling, forming a V–H pump. Ni and V as catalysts reduce the dissociation energy of H molecules on the surface of Mg and improve the kinetic performance of the H absorption reaction, and the unsaturated electron layer of Ni and V interacting with the valence electrons of H weaken the Mg-bonds, improving the kinetic performance of the H release reaction. Meanwhile, the interfacial effects of uniformly distributed Ni and V-O provide many active nucleation sites, which enhance H diffusion and hydride nucleation, ensuring that the catalyst is uniformly mixed with MgH_2 . In addition, the synergistic effect of the multi-metallic catalysts inhibit the in-situ synthesis of Mg_2NiH_4 and V-H from Mg/ MgH_2 , which jointly promotes the dehydrogenation reaction. During the H absorption/dehydrogenation reaction, V-O reacts with MgH_2 , leading to the formation of elemental V. The H_2 in MgH_2 is desorbed from the surface and MgH_2 is reduced to Mg; moreover, the H ions become H gas and escape from the surface of MgH_2 .

4. Conclusions

In summary, a NiCo-MOF/V-O (MOF, metal–organic framework) composed of V-O and a NiCo layered double hydroxide (LDH) was prepared using a hydrothermal method. It was found that vanadium promotes incorporation of the NiCoLDH into the MOF, causing the generation of defects and voids. The resulting composite was used to enhance the

hydrogen storage properties of MgH₂. More specifically, it was found that NiCo-MOF/V-O exhibited excellent catalytic properties and greatly enhanced the hydrogen release performance of MgH₂. This was evident by the fact that the MgH₂ composite containing 7 wt.% NiCo-MOF/V-O exhibited a lower hydrogen release temperature (155 °C) than pure MgH₂ after ball milling. Furthermore, at 300 °C, the hydrogen storage material released 6.4 wt.% H₂ in 200 s, reaching almost complete dehydrogenation after 5 min, with a dehydrogenation capacity of ~6.56 wt.%. Notably, these results provide fresh insights for the large-scale application of MgH₂ in changing the original LDH into a MOF structure, but there is a limitation such as the inability to change its thermodynamic properties. In subsequent studies, other metal salt solutions can be tried or even liquid infiltration of metal salt solutions into the MOF structure to investigate its hydrogen storage performance against MgH₂ or directly with MOFs materials tested for hydrogen storage in a low-temperature environment.

Declaration of competing interest

The authors declare that they have no known competing financial interests or personal relationships that could have appeared to influence the work reported in this paper.

CRediT authorship contribution statement

Zexuan Yang: Writing – original draft, Data curation, Conceptualization. **Yazhou Wang:** Writing – review & editing, Formal analysis. **Xia Lin:** Writing – review & editing, Formal analysis. **Yongjin Zou:** Writing – review & editing, Formal analysis, Conceptualization. **Cuili Xiang:** Writing – review & editing, Supervision, Formal analysis. **Fen Xu:** Writing – review & editing, Formal analysis. **Lixian Sun:** Writing – review & editing, Formal analysis. **Yong Shen Chua:** Writing – review & editing, Formal analysis.

Acknowledgments

This work was financially supported by the **National Natural Science Foundation of China** (Grant Nos. U24A2044, 52071092).

Supplementary materials

Supplementary material associated with this article can be found, in the online version, at doi:10.1016/j.jma.2025.01.012.

References

- [1] G.W. Crabtree, M.S. Dresselhaus, *MRS Bull* 33 (2008) 421–428.
- [2] M. Dornheim, N. Eigen, G. Barkhordarian, T. Klassen, R. Bormann, *Adv. Eng. Mater.* 8 (2006) 377–385.
- [3] Z. Ding, Y. Li, H. Yang, Y. Lu, J. Tan, J. Li, Q. Li, Y. Chen, L.L. Shaw, F. Pan, *J. Magnes. Alloys* 10 (2022) 2946–2967.
- [4] L. Zeng, Z. Lan, B. Li, H. Liang, X. Wen, X. Huang, J. Tan, H. Liu, W. Zhou, J. Guo, *J. Magnes. Alloy.* 10 (2022) 3628–3640.
- [5] Z. Ding, H. Li, L. Shaw, *Chem. Eng. J.* 385 (2020) 123856.
- [6] Z. Ding, Y. Lu, L. Li, L. Shaw, *Energy Storage Mater.* 20 (2019) 24–35.
- [7] H. Yang, Z. Ding, Y. Li, S. Li, P. Wu, et al., *Rare Met.* 42 (2023) 2906–2927.
- [8] J. Yang, A. Sudik, C. Wolverton, D.J. Siegel, *Chem. Soc. Rev.* 39 (2010) 656–675.
- [9] I. Staffell, D. Scamman, A.V. Abad, P. Balcombe, P.E. Dodds, P. Ekins, N. Shah, K.R. Ward, *Energy Environ. Sci.* 12 (2019) 463–491.
- [10] M.G. Rasul, M.A. Hazrat, M.A. Sattar, M.I. Jahirul, M.J. Shearer, *Energy Convers. Manage.* 272 (2022) 116326.
- [11] X. Zhang, Y. Liu, Z. Ren, X. Zhang, J. Hu, Z. Huang, Y. Lu, M. Gao, H. Pan, *Energy Environ. Sci.* 14 (2021) 2302–2313.
- [12] Y. Pang, Y. Liu, M. Gao, L.Z. Ouyang, J. Liu, H. Wang, M. Zhu, H. Pan, *Nat. Commun.* 5 (2014) 3519.
- [13] Y. Liu, K. Zhong, K. Luo, M. Gao, H. Pan, Q. Wang, *J. Am. Chem. Soc.* 131 (2009) 1862–1870.
- [14] Z. Ma, S. Panda, Q. Zhang, F. Sun, D. Khan, W. Ding, J. Zou, *Chem. Eng. J.* 406 (2021) 126790.
- [15] X. Zhang, Y. Liu, X. Zhang, J. Hu, M. Gao, H. Pan, *Mater. Today Nano* 9 (2020) 100064.
- [16] S.K. Verma, M.A. Shaz, T.P. Yadav, *Int. J. Hydrogen Energ.* 48 (2023) 21383–21394.
- [17] B. Ma, W. Jiang, L. Ouyang, H. Li, *Inorg. Chem. Front.* 10 (2023) 6879–6891.
- [18] B. Ma, C. Tan, L. Ouyang, H. Shao, N. Wang, M. Zhu, *J. Alloy. Compd.* 918 (2022) 165803.
- [19] B. Ma, L. Ouyang, J. Zheng, *J. Magnes. Alloy.* 12 (10) (2024) 4191–4204.
- [20] N.A. Ali, N.A. Sazelee, M. Ismail, *Int. J. Hydrogen Energ.* 46 (2021) 31674–31698.
- [21] F. Qureshi, M. Yusuf, M.A. Khan, H. Ibrahim, B.C. Ekeoma, H. Kamyab, M.M. Rahman, A.K. Nadda, S. Chelliapan, *Fuel* 340 (2023) 127574.
- [22] S.K. Pandey, S.K. Verma, A. Bhatnagar, T.P. Yadav, *Int. J. Energ. Res.* 46 (2022) 17602–17615.
- [23] Y. Shang, C. Pistidda, G. Gizer, T. Klassen, M. Dornheim, *J. Magnes. Alloy.* 9 (2021) 1837–1860.
- [24] L. Ouyang, L. Zhong, H. Liu, J. Wang, H. Shao, H. Huang, Z. Zhu, Min, *Angew. Chem. Int. Ed.* 59 (2020) 8623–8629.
- [25] L. Ouyang, W. Chen, J. Liu, M. Felderhoff, H. Wang, M. Zhu, *Adv. Energy Mater.* 7 (2017) 1700299.
- [26] Y. Liu, H. Du, X. Zhang, Y. Yang, M. Gao, H. Pan, *Chem. Commun.* 52 (2016) 705–708.
- [27] H. Pan, Y. Liu, M. Gao, Y. Zhu, Y. Lei, Q. Wang, *J. Alloy. Comd.* 351 (2003) 228–234.
- [28] Y. Liu, H. Pan, M. Gao, Q. Wang, *J. Mater. Chem.* 21 (2011) 4743–4755.
- [29] S. Shen, L. Ouyang, J. Liu, H. Wang, X. Yang, M. Zhu, *J. Magnes. Alloy.* 11 (2023) 3174–3185.
- [30] S. Shen, W. Liao, Z. Cao, J. Liu, H. Wang, L. Ouyang, *J. Mater. Sci. Technol.* 178 (2024) 90–99.
- [31] S. Dong, C. Li, J. Wang, H. Liu, Z. Ding, Z. Gao, W. Yang, W. Lv, L. Wei, Y. Wu, H. Li, *J. Mater. Chem. A* 10 (2022) 22363–22372.
- [32] C. Zhou, Y. Peng, Q. Zhang, *J. Mater. Sci. Technol.* 50 (2020) 178–183.
- [33] X. Ding, R. Chen, X. Chen, H. Fang, Q. Wang, Y. Su, J. Guo, *J. Magnes. Alloy.* 11 (2023) 903–915.
- [34] X. Pang, L. Ran, Y. Chen, Y. Luo, F. Pan, *J. Magnes. Alloy.* 10 (2022) 821–835.
- [35] Y. Zhang, X. Wang, C. Niu, D. Wang, Q. Shen, Y. Gao, H. Zhou, Y. Zhang, Y. Zhang, L. Dong, *Biosaf. Health* 4 (2022) 321–329.
- [36] V.C. Verma, S.K. Gond, A. Kumar, A. Mishra, R.N. Kharwar, A.C. Gange, *Microb. Ecol.* 57 (2009) 749–756.
- [37] S.K. Verma, M.A. Shaz, T.P. Yadav, *Int. J. Hydrogen Energ.* 48 (2023) 21383–21394.
- [38] Z. Peng, Q. Li, J. Sun, K. Chen, W. Jiang, H. Wang, J. Liu, L. Ouyang, M. Zhu, *J. Alloys Compd.* 891 (2022) 161791.

- [39] C. Zhou, K. Li, T. Huang, P. Sun, L. Wang, Y. Lu, Z.Z. Fang, Mater. Design 218 (2022) 110729.
- [40] N. Rambhujun, K.F. Aguey-Zinsou, Int. J. Hydrogen Energy 46 (2021) 28675–28685.
- [41] S. Rivoirard, P. de Rango, D. Fruchart, J. Charbonnier, D. Vempaire, J. Alloy. Compd. 356–357 (2003) 622–625.
- [42] X. Mao, Y. Zou, F. Xu, L. Sun, C. Xiang, ACS Appl. Mater. Interfaces 13 (2021) 22664–22675.
- [43] P. Chen, J. Ye, H. Wang, L. Ouyang, M. Zhu, J. Alloys Compd. 883 (2021) 160833.
- [44] M. Ma, L. Ouyang, J. Liu, H. Wang, H. Shao, M. Zhu, J. Power Sources 359 (2017) 427–434.
- [45] P. Zou, W. Jiang, L. Ma, L. Ouyang, J. Mater. Chem. A 12 (2024) 11960–11967.
- [46] S. Gong, L. Zhang, G. Zhao, L. Ouyang, J. Alloy. Compd. 986 (2024) 174026.
- [47] S. Guo, C. Pang, P. He, X. He, J. Ren, L. Ouyang, Appl. Surf. Sci. 651 (2024) 159255.
- [48] H. Zhong, K. Chen, C. Qin, C. Lang, J. Liu, H. Wang, J. Zhang, L. Ouyang, J. Alloy. Compd. 976 (2024) 173160.
- [49] Q. Li, Z. Peng, W. Jiang, L. Ouyang, H. Wang, J. Liu, M. Zhu, J. Alloys Compd. 889 (2021) 161629.
- [50] C. Lu, J. Zou, X. Zeng, W. Ding, Int. J. Hydrogen Energy 42 (2017) 15246–15255.
- [51] G. Liang, J. Huot, S. Boily, A. Van Neste, R. Schulz, J. Alloys Compd. 292 (1999) 247–252.
- [52] Y. Meng, J. Zhang, S. Ju, Y. Yang, Z. Li, F. Fang, D. Sun, G. Xia, H. Pan, X. Yu, J. Mater. Chem. A 11 (2023) 9762–9771.
- [53] Z. Lu, J. He, M. Song, Y. Zhang, F. Wu, J. Zheng, L. Zhang, L. Chen, Int. J. Miner. Metall. Mater. 30 (2023) 44–53.
- [54] J. Gao, Y. Hu, Y. Wang, X. Lin, K. Hu, X. Lin, G. Xie, X. Liu, K.M. Reddy, Q. Yuan, H. Qiu, Small 17 (2021) 2104684.
- [55] J. Wu, Z. Yu, Y. Zhang, S. Niu, J. Zhao, S. Li, P. Xu, Small 17 (2021) 2105150.
- [56] W. Liu, T. Gao, Y. Yang, Q. Sun, Z. Fu, Phys. Chem. Chem. Phys. 15 (2013) 15806.
- [57] E. Yilmaz, C. Yogi, K. Yamanaka, T. Ohta, H.R. Byon, Nano Lett. 13 (2013) 4679–4684.
- [58] Y. Baba, T.A. Sasaki, J. Nucl. Mater. 132 (1985) 173–180.
- [59] G. Silversmit, D. Depla, H. Poelman, G.B. Marin, R. De Gryse, J. Electron Spectrosc. 135 (2004) 167–175.
- [60] E. Hryha, E. Rutqvist, L. Nyborg, Surf. Interface Anal. 44 (2012) 1022–1025.
- [61] S. Wang, Y. Zou, F. Xu, C. Xiang, H. Peng, J. Zhang, L. Sun, J. Energy Storage 41 (2021) 102862.
- [62] J. Wu, Z. Liu, H. Zhang, Y. Zou, B. Li, C. Xiang, L. Sun, F. Xu, T. Yu, J. Magnes. Alloys (2024).
- [63] Y. Lu, Y. Qin, M. Chen, G. Liu, P. Qi, H. Wu, Y. Tang, Appl. Surf. Sci. 611 (2023) 155625.
- [64] X. Wen, H. Liang, R. Zhao, F. Hong, W. Shi, H. Liu, H. Chen, W. Zhou, J. Guo, Z. Lan, J. Mater. Chem. A 10 (2022) 16941–16951.
- [65] S. Guemou, F. Wu, P. Chen, J. Zheng, T. Bian, D. Shang, A.P. Levtssev, L. Zhang, Int. J. Hydrogen Energy 48 (2023) 23943–23955.
- [66] H. Liu, X. Duan, Z. Wu, H. Luo, X. Wang, C. Huang, Z. Lan, W. Zhou, J. Guo, M. Ismail, Chem. Eng. J. 468 (2023) 143688.
- [67] K.C. Tome, S. Xi, Y. Fu, C. Lu, N. Lu, M. Guan, S. Zhou, H. Yu, Int. J. Hydrogen Energy 47 (2022) 4716–4724.
- [68] Q. He, W. Sun, H. Li, Y. Wang, C. Yin, C. Xiang, Y. Zou, F. Xu, L. Sun, J. Alloys Compd. 1009 (2024) 176975.
- [69] A.M. Lakhnik, I.M. Kirian, A.D. Rud, Int. J. Hydrg. Energy 47 (2022) 7274–7280.
- [70] L. Zhang, F.M. Nyahuma, H. Zhang, C. Cheng, J. Zheng, F. Wu, L. Chen, Green Energy Environ. 8 (2023) 589–600.
- [71] G. Tian, F. Wu, H. Zhang, J. Wei, H. Zhao, L. Zhang, J. Phys. Chem. Solids 174 (2023) 111187.
- [72] Z. Lu, H. Yu, X. Lu, M. Song, F. Wu, J. Zheng, Z. Yuan, L. Zhang, Rare Met. 40 (2021) 3195–3204.
- [73] L. Zhang, K. Wang, Y. Liu, X. Zhang, J. Hu, M. Gao, H. Pan, Nano Res. 14 (2021) 148–156.
- [74] E. Hryha, E. Rutqvist, L. Nyborg, Surf. Interface Anal. 44 (2012) 1022–1025.
- [75] H.F. Franzen, G.A. Sawatzky, J. Solid State Chem. 15 (1975) 229–232.
- [76] F. Werfel, O. Brümmer, Phys. Scr. 28 (1983) 92.
- [77] H. Zhong, L. Ouyang, J.S. Ye, J.W. Liu, H. Wang, X.D. Yao, M. Zhu, Energy Storage Mater. 7 (2017) 222–228.